Microstructure-based RVE modeling of the failure behavior and LCF resistance of ductile cast iron

Available online at www.sciencedirect.com

ScienceDirect

Procedia Structural Integrity 24 (2019) 324–336

Structural Integrity Procedia

www.elsevier.com/locate/procedia

AIAS 2019 International Conference on Stress Analysis

Microstructure-based RVE modeling of the failure behavior and LCF resistance of ductile cast iron

Luca Collini[a,*], Alessandro Pirondi[a]

[a]*Department of Engineering and Architecture, University of Parma*
Viale delle Scienze 181/A, 43124 Parma (Italy)

Abstract

In this work the failure behavior of ductile cast iron microstructure subjected to tensile and low-cycle fatigue loadings is simulated by a 3-D, FE Reference Volume Element approach. A fully ferritic matrix is considered as representative of the low-hardness, high-ductility material class of nodular cast irons. Plastic flow potential rule, ductile and low cycle fatigue damage models are implemented at the micro-scale for the matrix constituent in conjunction with nonlinear cyclic hardening laws, and periodic boundary conditions are imposed over the RVE at the meso-scale. Different values of triaxiality are imposed. Numerical results confirm experimental findings of the behavior at the meso-scale and correctly predict the LCF lifetime, driving the interpretation of inner strain distribution, voids interaction and triaxiality effects on failure mechanisms.

Keywords: Ductile cast iron; RVE; Ductile damage model; Triaxiality; Low-cycle fatigue.

1. Introduction

Nodular, or ductile cast iron (DCI), presents the peculiar characteristics of the graphite precipitated in tiny balls or spheroids. Spheroids interrupt the iron matrix much less than graphite flakes, as occurring in gray cast iron, resulting in higher strength and toughness, i.e. ductility. Subsequently its use in widespread for the production of many industrial parts which include crankshafts, gears, rocker arms and disc brake calipers.

* Corresponding author. Tel.: +39-0521-905892; fax: +39-0521-905705.
E-mail address: luca.collini@unipr.it

10.1016/j.prostr.2020.02.030

Nomenclature

a	Mean half interparticle spacing
ψ_G	graphite volume fraction
ψ_F	ferrite volume fraction
N	nodule count
d_G	nodule average diameter
K_{ti}	elastic stress concentration factor along the i-direction, i = 1, 2, 3
σ^0	yield stress
A, B	parameters of Johnson-Cook hardening law
n	hardening exponent
K_i	parameters of ductile damage model, i = 1, 2, 3
p	first stress invariant (hydrostatic pressure)
q	second stress invariant (equal to von Mises equivalent stress, σ_{eq})
η	local stress triaxiality $\eta = -p/q$
$\bar{\varepsilon}_D^{pl}$	equivalent plastic strain at the onset of damage in ductile criterion
$\bar{\varepsilon}_f^{pl}$	equivalent strain at failure
ω_D, D	damage variables
l	RVE size
L_{EL}	Finite element characteristic length
c_i	material damage parameters, i = 1,…,4
Σ_{ij}	stresses at the meso-scale
T	stress triaxiality at the meso-scale
E_f^{pl}	RVE failure strain
Υ_f^{pl}	RVE failure displacement
E_a	cyclic strain amplitude at the meso-scale
N_0	number of cycles to failure

The static strength of DCI is comparable to cast steels, and fatigue strength and ductility are much greater than grey irons. Castability and machinability are also good, and all these properties makes it an economic alternative for medium stressed components and for safety critical applications. A reduction of 30% or more in component cost can be made when nodular iron is substituted for cast or forged steel, Hamberg et al. (1997).

As said, the peculiar structure of DCI motivated in the past the study of plasticity and damage in ductile solids, with the aim of developing material damage models. In many experiments, the microstructural features are correlated to ductility, static and fatigue strength, and toughness, see for example Bradley et al. (1990), Tartaglia et al. (2000), Berdin et al. (2001), Hafiz (2001), Nicoletto et al. (2002, 2004, 2006), Collini et al. (2005), Lacaze et al. (2016). From the modeling point of view, instead, starting from the work by Needleman (1987, 1991), the DCI structure served as test field for calibration of damage models based on nucleation, growth and coalescence of cavities in a high-volume fraction solid, see for example Zhang et al. (1996). The interaction between closely spaced voids on the kinetics of the damage mechanism is also studied, see for example Dong et al. (1997), Ghahremaninezhad et al. (2012), Dahlberg et al. (2014), Hütter et al. (2015), Guillermer-Neel et al. (2000), and an attempt is made to define quantitative parameters accounting for the free path between the nodules, or by applying a critical void volume fraction concept. Also, thermal residual stresses are demonstrated to influence the non-linear behavior in the early deformation range, Bonora et al. (2005).

The fatigue behavior in the short cycle regime (LCF), i.e. at high diffused plasticity, is also studied in several works: experimentally, see Harada et al. (1992), Komotori et al. (1998), Atzori et al. (2012), Canzar et al. (2012), Meneghetti et al. (2014), Ricotta (2015), Bleicher et al. (2017), and by numerical approaches based on such evidences, for example Lukhi et al. (2018), Rabold et al. (2005). Ferritic DCI generally shows a hardening behavior under strain-

controlled tests, that depend on the applied plastic strain amplitude. A specific Bauschinger effect characterized by a high internal stress and an unusual hysteresis loop shape is also observed, and explained by inhomogeneities in deformation between inclusions and matrix and the development of enhanced dislocation density in the matrix from the interface, Petrenec et al. (2010). However, similarly to the tensile loading, the damage process under LCF loading starts at the cavities/matrix interface by the accumulation of dislocations arranging in 45° inclined paths, which cause the crack formation for the incompatibility of deformation, Guillemer-Neel et al. (1999).

Nevertheless, not all the observed mechanisms of damage and failure in DCI are fully understood yet. For example, peculiar configurations of the nodule cavities can influence the ductility, and make it possible the development of brittle fracture features even in the extremely ductile matrix. Yanagisawa et al. (1983) tried to model the ductility reduction defining a parameter $\eta = 1/3 + a/d_G$ related to the distance-on-size ratio of nodules, which locally determines significant deviation from the imposed "external" triaxiality, i.e. 1/3 in the case of uniaxial traction. Anyway, different triaxiality states are found very commonly in the industrial application, for example in proximity of a notch, which concentrates the stresses and tends to create higher triaxialities.

On the other hand, many experimental tests on steels and alloyed steels show how deeply the ductility is influenced by the stress triaxiality, being usually reduced when the triaxiality increases, see for example Hradil et al. (2017), and Bai et al. (2008). To the knowledge of the authors, these tests are completely missing for the DCI.

Regarding the LCF behavior, the cyclic properties and some peculiar phenomenon as the Bauschinger effect, ferritic DCI still deserves investigation, being partially unknown the role of the population of cavities.

Hence, the aim of this work is to study the damage mechanism of DCI and the effect of stress triaxiality on the ductility at failure. This is made by a FE, RVE modeling approach, which faithfully reproduce a real microstructural configuration. In fact, random arrangements of graphite nodule cavities are created inside the RVE, periodic boundary conditions are applied and plasticity rules and damage evolution laws are given to the matrix at the microscale, while different triaxialities are imposed at the RVE boundaries on the mesoscale.

The same model is tested applying a phenomenological damage model for the LCF fatigue based on the hysteresis energy, and applying controlled strain amplitudes.

The results show a very good agreement with the experimental data available at a triaxiality value of 1/3, predict the effect of a wide range of imposed triaxialities on the ductility, and correctly interpret the LCF life when compared with literature data. Details of plastic strain concentration and initiation of damage are also given.

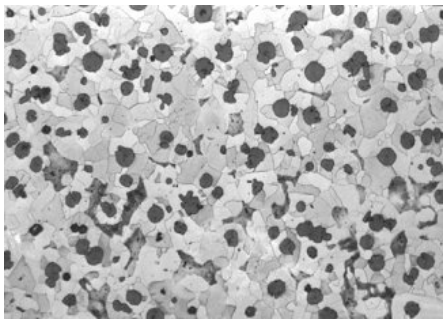

Fig. 1. Full ferritic DCI microstructure (etched, X100).

2. Microstructure and RVE model

The full ferritic microstructure shown in the micrographs of Fig. 1 is here taken into consideration. The chemical composition is reported in Tab. 1, where the Equivalent Carbon content CE[1] is also indicated. Microstructural and strength data are also reported in Tab. 1.

[1] The CE concept is used to understand how alloying elements will affect the heat treatment and casting behavior. CE = %C + 0.33 (%Si + %P).

Table 1. Chemical composition and mechanical properties of considered DCI, from Nicoletto et al. (2002).

C	S	P	Si	Mn	Cr	Ni	Mo	Al	Cu	Mg	Ti	Ce	Sn	CE
3,69	0,01	0,063	3,10	0,26	0,04	-	-	-	-	0,046	-	-	-	4,74

Graphite form	N (mm^{-1})	ψ_G (%)	ψ_F (%)	E (GPa)	σ^0 (MPa)	σ^u (MPa)	ε^{pl}_f (%)	KC0 (J/cm^2)	HB
80%VI7+20%V7	174	15.0	93.5	162	350	535	15	90	178

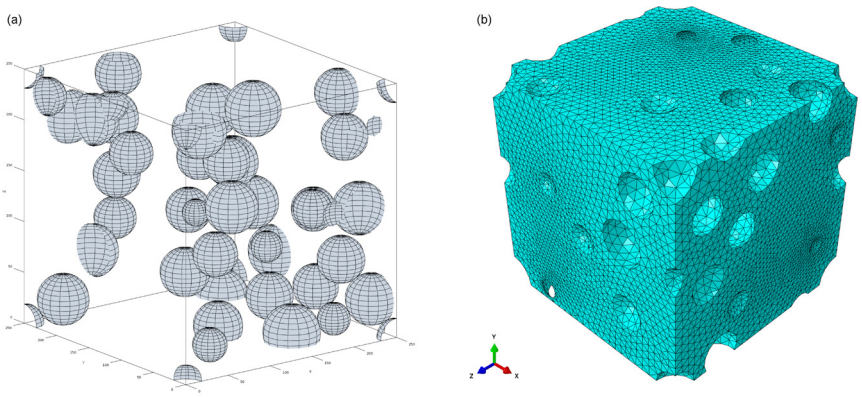

Fig. 2. RVE model: (a) statistical generation of voids; (b) finite element meshed solid.

One can notice that graphite is 15% in volume and form regular spheroids, and that the material preserves a high ductility. Ferrite grains are of the same size order of the spheroids, being in the range of 50÷150 μm. As already said, the damage mechanism corresponds essentially to strain localization around the nodules that act as voids because of the scarce adhesion with the iron matrix, formation of microvoids and coalescence. Under certain circumstances or for mixed ferritic/pearlitic matrixes, traces of cleavage facets can even be found in the ferrite surrounding the nodules. However, the damage originates into the matrix at the microstructural scale.

In this study to model the DCI material system a Reference Model Volume (RVE) approach is chosen, due to its peculiarities. The RVE is a "small" volume statistically representative, for it contains any peculiar element at the microstructural level, and it should be as small as possible in order to reduce the calculation time, Collini (2010), Kanita et al. (2003). Inside the RVE, here shown in Fig. 2, graphite nodules are modeled as spherical voids of various size. A cubic RVE of size $l = 0.250$ mm is defined containing random configuration of the voids, as indicated in Tab. 2. For this purpose, it is used the open-source toolbox Mote3D developed by Richter (2017), which automatically creates a population of spherical particles with user-defined characteristics, and periodicity. The RVE generated is imported in the Abaqus™ CAE model by Python-based script, and meshed by tetrahedral linear elements, with the data indicated in Tab. 2. Finite element simulations are performed imposing a homogeneous stress or strain field under periodic boundary conditions; for this purpose, Abaqus™ provides the powerful functionality of a Micromechanics plugin developed by Omairey et al. (2019). The plugin post processing includes the calculation of the RVE homogenized properties from the completed analysis as well as performing averaging and statistical analysis of the fields in the whole volume and within individual constituents.

Table 2. Modeling features and parameters used for the ferrite.

N	d_G (μm)	Nodes	Elements	L_{EL} (mm)	P (kg/mm^3)	E (GPa)	ν	A (MPa)	B (MPa)	n	m	$\bar{u}^{pl}_f$	A	c_1	c_2	c_3	c_4
49	45 ± 8	53,657	268,313	0.0103	7,85e-6	206	0.3	560	625	0.50	0	0.0015	10	47297	-2.198	10^{-3}	2.5

The control of the stress triaxiality over the cell is crucial, Lin et al. (2006). In this work, it is made on the meso-scale of the RVE, imposing the meso-stresses Σ_{ij} according to the general definition of triaxiality T:

$$T = \frac{\Sigma_m}{\Sigma_{eq}} = \frac{\frac{1}{3}\left(\Sigma_{11}+\Sigma_{22}+\Sigma_{33}\right)}{\frac{1}{\sqrt{2}}\sqrt{\left(\Sigma_{11}-\Sigma_{22}\right)^2+\left(\Sigma_{22}-\Sigma_{33}\right)^2+\left(\Sigma_{11}-\Sigma_{33}\right)^2}} \tag{1}$$

In this study several triaxiality values of are considered and imposed by imposing uniform tractions Σ_{ij} at the boundaries. The RVE failure strain E_f^{pl} is then determined as the maximum displacement $\Upsilon_{f,i}^{pl}$ along the direction j reached by the simulation before degradation, relative to the cell dimension l_j and under the triaxiality T_i, Eq. (2):

$$\mathrm{E}_f^{pl}\Big|_{T_i} = \frac{\Upsilon_{f,ij}^{pl}}{l_j} \tag{2}$$

3. Modeling of damage

3.1. Ductile damage

A classical plasticity model is chosen to reproduce the plastic flow of the ferrite. Isotropic hardening with a Mises-type yield surface, associated flow rule and a Johnson-Cook hardening law is used, where the yield stress, σ^0, is assumed to be of the form:

$$\sigma^0 = \left[A + B\left(\bar{\varepsilon}^{pl}\right)^n\right]\left(1-\hat{\theta}^m\right) \tag{3}$$

The parameters *A, B* and the hardening exponent *n* are taken from the literature for a α-ferrite Fe-Si matrix, Springer (2012). The values are reported in Tab. 2 and in a graphical form in Fig. 3(a).

The damage process is here reproduced by the Abaqus™ ductile damage model, which is a phenomenological model for predicting the onset of damage due to nucleation, growth, and coalescence of voids. The model assumes that the equivalent plastic strain at the onset of damage $\bar{\varepsilon}_D^{pl} = f\left(\eta, \dot{\varepsilon}_D^{pl}\right)$ is a function of the stress triaxiality and strain rate, where $\eta = -p/q$ is the local stress triaxiality with p the hydrostatic pressure and q the deviatoric stress at the micro-scale. The damage initiation is satisfied when:

$$\omega_D = \int \frac{d\bar{\varepsilon}^{pl}}{\bar{\varepsilon}_D^{pl}\left(\eta, \dot{\varepsilon}_D^{pl}\right)} = 1 \tag{4}$$

where ω_D is a state variable that increases monotonically as $\Delta\omega_D$ increases with the plastic deformation for each increment of plastic strain $\Delta\bar{\varepsilon}_D^{pl}$. In this study, for the ferritic phase the fracture strain vs. stress triaxiality dependence is assumed to be an exponential law of the Johnson-Cook type:

$$\varepsilon_D^{pl} = \mathrm{K}_1 + \mathrm{K}_2\, \mathrm{e}^{-\mathrm{K}_3\eta} \tag{5}$$

The parameters in Eq. (5) are reported in Tab. 2, and the represented in graphical form is depicted in Fig. 3(b). This assumption is supported by behavior of α-ferrite and ferritic steels observed in experimental tests under variable triaxiality conditions, see Johnson et al. (1985), Mirza et al. (1996), Maresca (1997), Hopperstad et al. (2003), Bao et al. (2004), Springer (2012), Hradil et al. (2017). For negative stress triaxiality values, if no data are available no dependency is assumed and failure strain is kept constant, Manjoine (1982).

Once the initiation criterion of Eq. (4) is satisfied, the material stiffness is progressively degraded according to a specified damage evolution law for the criterion, having effect on the material response and eventually leading to the material failure. Here, Abaqus™ assumes that the degradation follows a scalar damage variable, D, and at any given time during the analysis the stress tensor is computed. The material loses its load-carrying capacity when $D = 1$, and now on the element is removed from the mesh. The plastic displacement measure $\dot{\bar{u}}^{pl}$ (which is mesh-dependent from the element characteristic length L_{EL}, $\dot{\bar{u}}^{pl} = L_{EL}\dot{\bar{\varepsilon}}^{pl}$) is used to drive the evolution of damage after damage initiation, by an exponential softening type with exponent α and the maximum degradation option set (values reported in Tab. 2).

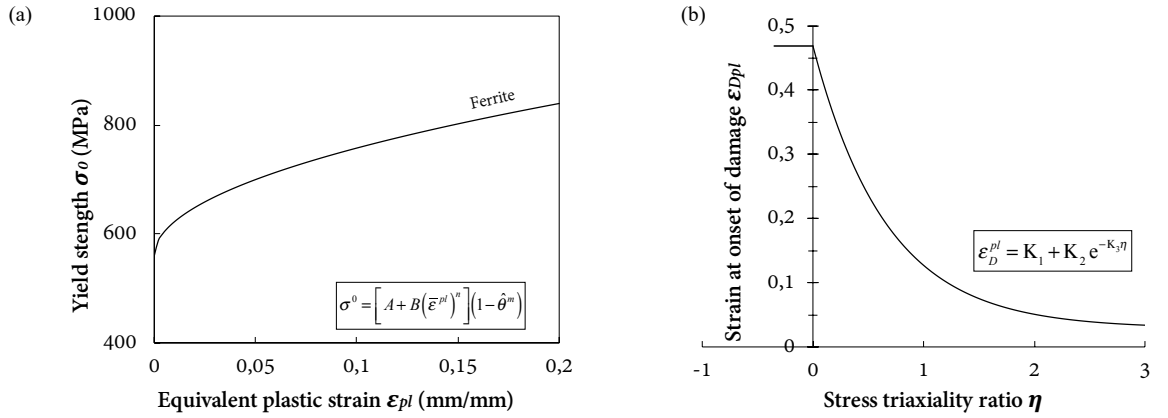

Fig. 3. Constitutive laws for the ferrite: (a) plastic flow rule; (b) failure strain vs. stress triaxiality.

3.2. Nonlinear isotropic/kinematic hardening model

A nonlinear isotropic/kinematic model is implemented to reproduce the cyclic behavior of ferritic matrix. The evolution law of this model consists of two components: a nonlinear kinematic hardening component, which describes the translation of the yield surface in stress space through the backstress α, and an isotropic hardening component, which describes the change of the equivalent stress defining the size of the yield surface, σ^0, as a function of plastic deformation. The kinematic hardening component is defined to be an additive combination of a purely kinematic term and a relaxation term, which introduces the nonlinearity:

$$\alpha = C\frac{1}{\sigma^0}(\boldsymbol{\sigma} - \boldsymbol{\alpha})\dot{\bar{\epsilon}}^{pl} - \gamma\boldsymbol{\alpha}\dot{\bar{\epsilon}}^{pl} \tag{6}$$

where C and γ are material parameters here calibrated from cyclic test data, Canzar et al. (2012), Guillemer-Neel et al. (1999), with the results $C = 15{,}000$; $\gamma = 260$; $\alpha_1 = -130$.

The isotropic hardening behavior of the model defines the evolution of the yield surface size, σ^0, as a function of the equivalent plastic strain, $\bar{\epsilon}^{pl}$. This evolution is introduced by using the exponential law:

$$\sigma_0 = \sigma|^0 + Q_\infty\left(1 - e^{-b\bar{\epsilon}^{pl}}\right) \tag{7}$$

where $\sigma|^0$ is the yield stress at zero plastic strain and Q_∞ and b are material parameters here derived from the literature: $\sigma|^0$ =280 MPa, $Q_\infty = 49$ and $b = 2$.

In the kinematic hardening models, the center of the yield surface moves in stress space due to the kinematic hardening component. In addition, with the nonlinear isotropic/kinematic hardening model the yield surface range may expand or contract due to the isotropic component, allowing the modeling of inelastic deformation in metals that are subjected to cycling loading resulting in significant inelastic deformation and low-cycle fatigue failure. These models can account for the Bauschinger effect, and the cyclic hardening with plastic shakedown.

3.3. Modeling of LCF damage initiation and evolution

The fatigue damage is here prediceted by using a damage evolution law based on the inelastic strain energy when the material response is stabilized after some cycles. Because the computational cost, the Abaqus™ *direct cyclic* feature is used to evaluate the RVE response subjected to a small fraction of the actual loading history. This response is then extrapolated over many load cycles using empirical formulae such as the Coffin-Manson relationship to predict the likelihood of crack initiation and propagation.

The direct cyclic low-cycle fatigue procedure models the progressive damage and failure of the material, based on a continuum damage mechanics approach. The response is obtained by evaluating the behavior at discrete points along the loading history, and the solution at each of these points is used to predict the degradation and evolution of material properties that will take place during the next increment, which spans a number of load cycles. The degraded material properties are then used to compute the solution at the next increment in the load history.

The damage initiation criterion here adopted is a phenomenological model for predicting the onset of damage due to stress reversals and the accumulation of inelastic strain in the LCF analysis. It is characterized by the accumulated inelastic hysteresis energy per cycle in a material point, Δw, when the response is stabilized in the cycle. The cycle number in which damage is initiated is given by:

$$N_0 = c_1 \Delta w^{c_2} \tag{8}$$

where c_1 and c_2 are constants calculated by data (hysteresis loops) from literature, Canzar et al. (2012), and are here reported in Tab. 2. After damage initiation the elastic material stiffness is degraded progressively in each cycle based on the accumulated stabilized inelastic hysteresis energy, and the damage state is calculated and updated based on the inelastic hysteresis energy for the stabilized cycle. The rate of the damage in a material point per cycle is then given by the following model:

$$\frac{\mathrm{d}D}{dN} = \frac{c_3 \Delta w^{c_4}}{L_{EL}} \tag{9}$$

where c_3 and c_4 are again material constants, and L_{EL} is the characteristic length associated with an integration point, see Tab. 2. As for the ductile static damage, the degradation of the elastic stiffness is modeled using a scalar damage variable, D. At any given loading cycle during the analysis the stress tensor in the material is given by a scalar damage equation: the material has completely lost its load carrying capacity when $D = 1$. Elements are then removed from the mesh if all of the section points at all integration locations have lost their loading carrying capability. The graphical determination of $c_1,\ldots,c_4$ constants is illustrated in Fig. 4.

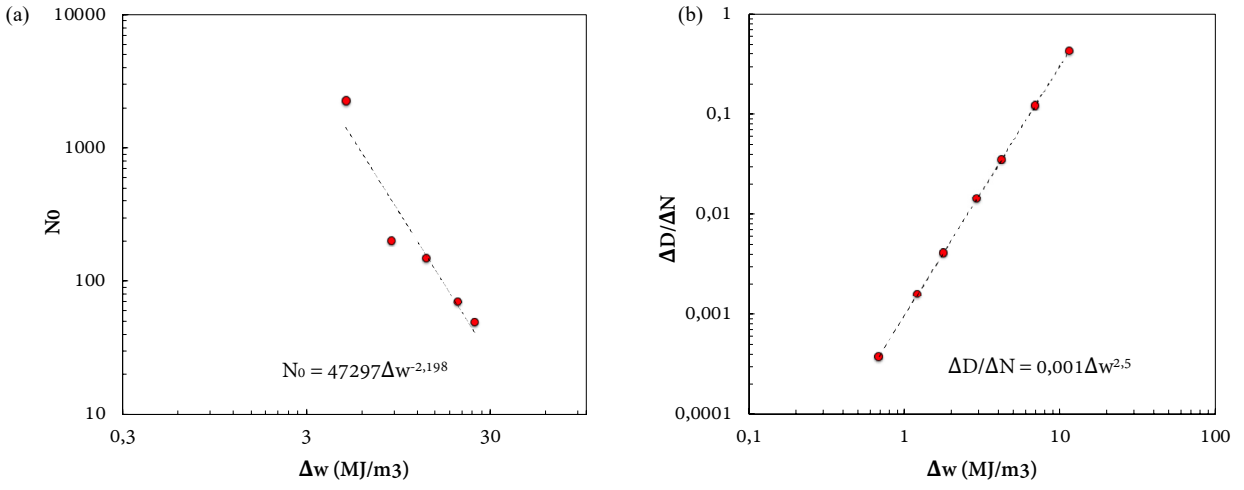

Fig. 4. (a) Number of cycles to failure, and (b) damage cumulation vs. hysteresis energy, elaborated from Canzar et al. (2012).

4. Results of simulations

4.1. Tensile response

Elastic properties of the RVEs are calculated by the homogenizing the response to traction in the three directions. The resulting engineering constants reported in Tab. 3 are close to the experimental with a maximum difference of 5% and variation between the three directions are within 2%. This result confirms that the chosen size of the RVE is acceptable. The maximum stress concentration factors exerted by the voids along the 3 directions, namely K_{t1}, K_{t2} and K_{t3}, are within the range 2÷2.6, which are higher that the single spherical void solution ($K_t = 2$). It is evident a void interaction effect, corresponding to an average distance between the nodules of about 1.2/1.3 times their diameter, see the work by Bidhar et al. (2011) for paired spherical cavities. Here nodules do not have the same diameter, however entering this value in the Yanagisawa model would give a local triaxiality estimation of (1/3 + 0.25) ≈ 0.6. As shown in the following, triaxiality developed in the RVE can be locally much higher when the plastic range is considered.

Table 3. Homogeneous elastic properties of RVEs (in GPa).

	E_{11}	E_{22}	E_{33}	G_{12}	G_{13}	G_{23}	ν_{12}	ν_{13}	ν_{23}	ρ (kg/m^3)	K_{t1}	K_{t2}	K_{t3}
Experimental	162.0	–	–	64.3	–	–	0.26	–	–	7.3	–	–	–
RVE	163.6	166.0	165.2	63.6	63.8	64.4	0.283	0.286	0.289	6.92	2.24	2.36	2.18

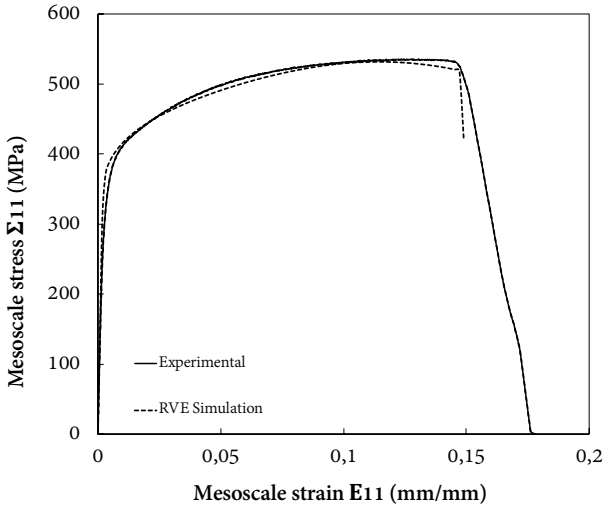

Fig. 5. Experimental and RVE simulated tensile response of ferritic DCI.

Tensile response of the RVE, see Fig. 5, is obtained by plotting the resulting nominal meso-stress Σ_{11} vs. the imposed elongation E_{11}. A very good agreement with the experimental nominal curve taken from Nicoletto et al. (2002) and Collini et al. (2005) is found, in the elastic range, at the onset of plasticity and in the strain hardening region. The simulation evidences more acutely the onset of necking, because of beginning of element stiffness degradation. The failure strain, here corresponding to the element removal, can be correctly tuned by the plastic displacement value at failure, $\dot{\bar{u}}^{pl} = L_{EL}\dot{\bar{\varepsilon}}^{pl}$.

4.2. Strain distribution and triaxiality

Maps of local total strain, stress and triaxiality are shown in the contours of Fig. 6, at the applied strain of 0.2%, 1% and 3%. Strain distribution looks extremely inhomogeneous, concentrating around the nodules, especially the smallest or the clustered ones. Triaxiality goes locally higher (from 0.6 to 1.7) once the plastic range is encountered.

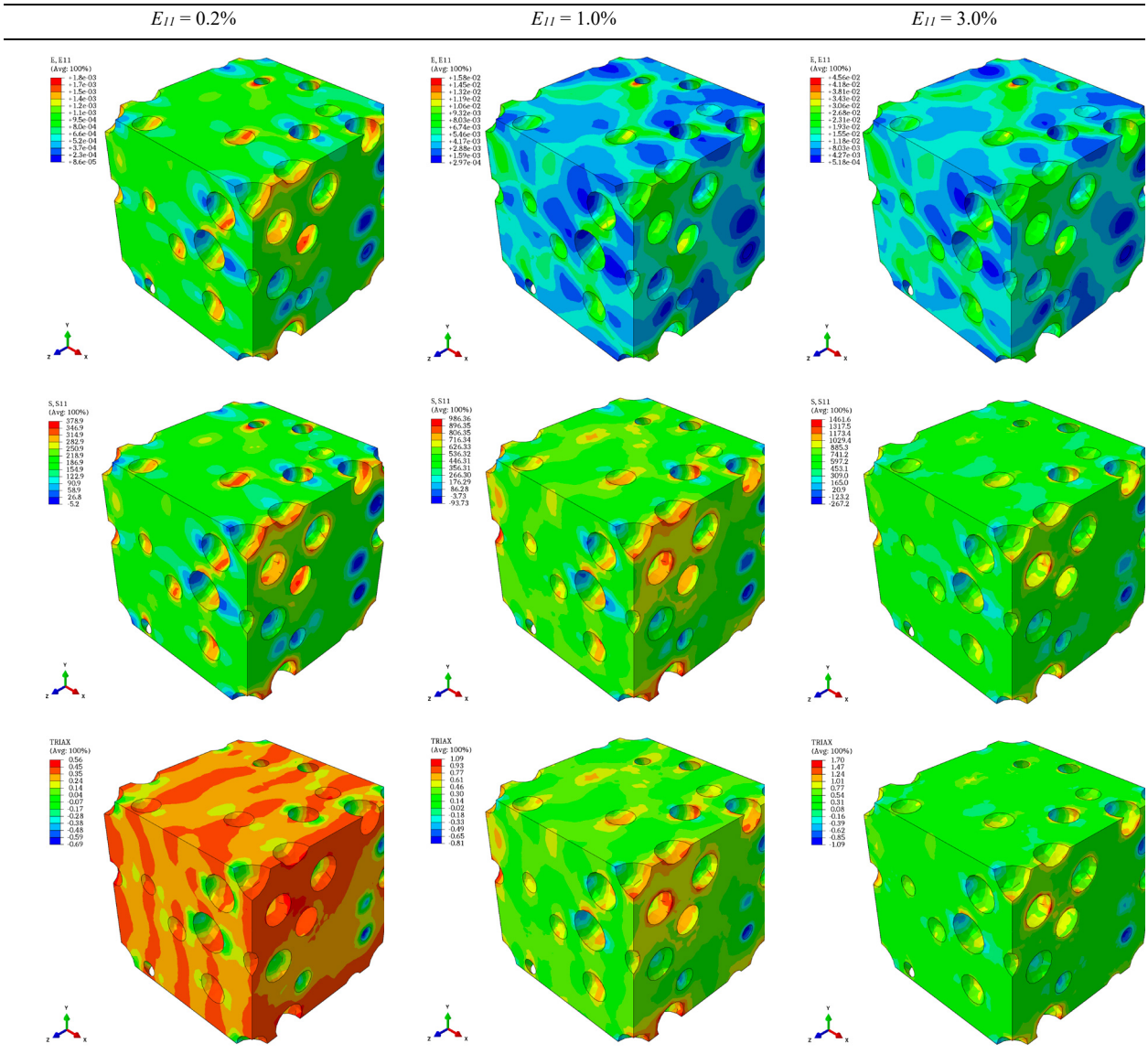

Fig. 6. Contours of strain ε_{11}, stress σ_{11}, and triaxiality η at applied mesoscopic strain equal to 0.2%, 1%, 3%.

The local damage variable ω_s, here shown in the sections of Fig. 7, concentrates where both the equivalent plastic strain and triaxiality concentrate, indicating that the damage starts where stresses become multiaxial. It's worth to notice that local developed triaxiality directly influences the failure strain of the matrix, promoting the rupture.

The results of the simulations on the failure strain as calculated by Eq. (2), are summarized in the plot of Fig. 8 for different triaxiality T imposed at the mesoscale. The RVE reaches the failure following the ferrite failure behavior, but decreased by the voids action described above. As previously seen from experiments, graphite nodules play a double role in decreasing the ductility of the matrix, since they concentrate the plastic strain and confine the strain itself creating local higher hydrostatic pressure. The few available experimental data on failure of ferritic DCI (GJS-400) at different triaxialities, taken from Memhard et al. (2011), agree with the prediction of the RVE model. High triaxiality state of stress is then demonstrated to have a detrimental effect on the material ductility, as qualitatively reported elsewhere, see Lin et al. (1994) and Di Cocco et al. (2013, 2014).

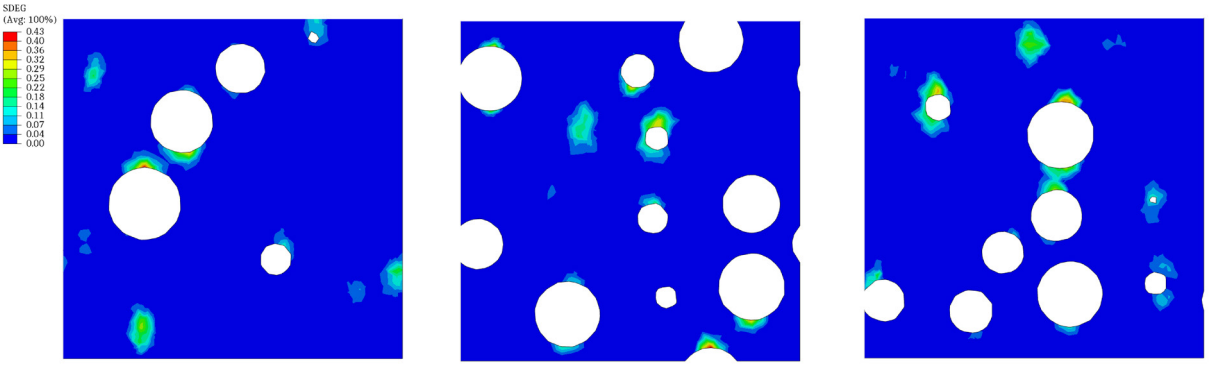

Fig. 7. Sections of the RVE showing the damage distribution (E_{11} = 8%).

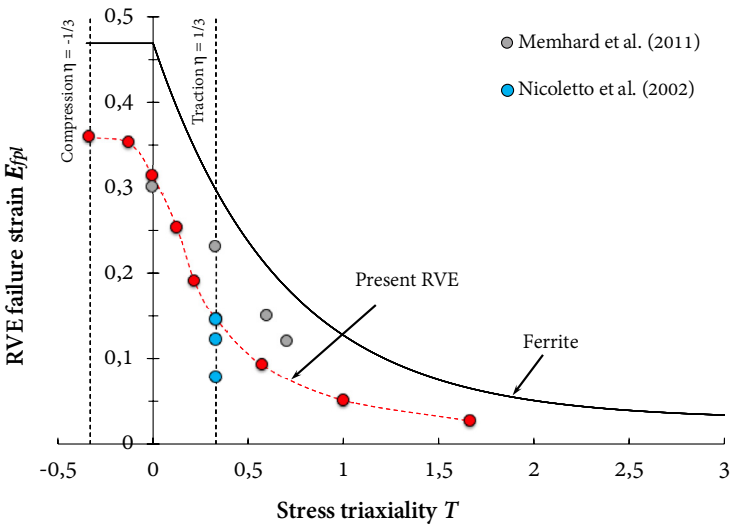

Fig. 8. Experimental and RVE simulated tensile response of ferritic DCI.

4.3. Cyclic loading

Four hysteresis loops originated by the FE calculation are compared with six experimental loops in Fig. 9. Loops are obtained plotting the nominal, mesoscopic stress Σ_{11} vs. mesoscopic strain amplitude $E_{a,11}$ of 0.40%, 0.80%, 1.00% and 1.20%, after the cycles have stabilized. The RVE calculation correctly determines the initial hardening behavior of DCI, and generally indicates a good agreement with the experimental hysteresis loops. It has to be said that due to the mesh-dependency, the code cannot calculate the hysteresis loop at very low strain amplitude, namely below 0.20–0.30%.

As said above, the FE code calculates the deformation energy related to the determined loop and correlates it with a number of cycles necessary to initiate the damage. The total number of cycles to failure is then determined by calculating the damage evolution up to the element removal. Results are summarized in the plot of Fig. 10 where are plotted the applied meso-scopic strain amplitude vs. the number of reversals to failure $2N_f$. The simulated curve fall within the experimental data on ferritic cast irons taken from Harada et al. (1992), Komotori et al. (1998), Tartaglia et al. (2000), Atzori et al. (2012), Ricotta (2015), Hoyer (2016) and Bleicher et al. (2017).

Finally, the map of damage distribution in a LCF analysis is shown on the right side of Fig. 10: again, damage localizes preferentially at clustered nodules.

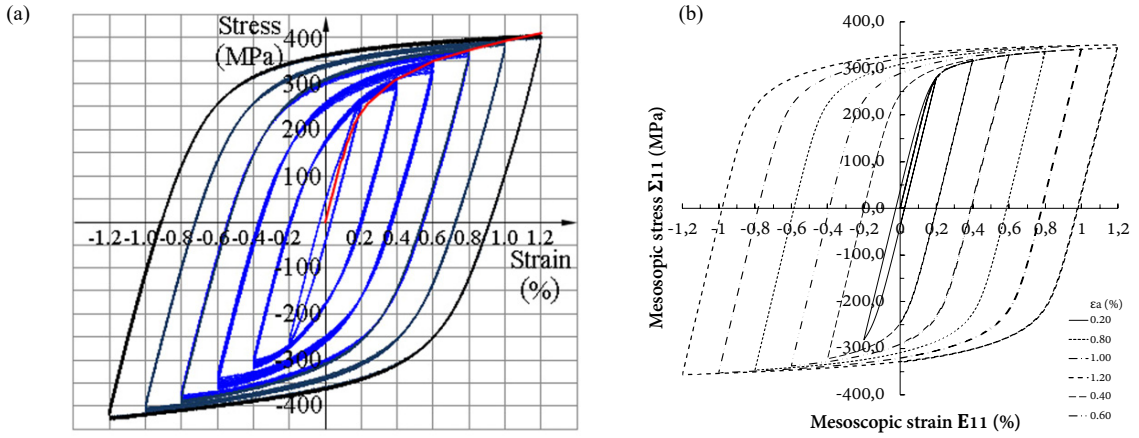

Fig. 9. Hysteresis cycles: (a) experimental, from Canzar et al. (2012); (b) present RVE model.

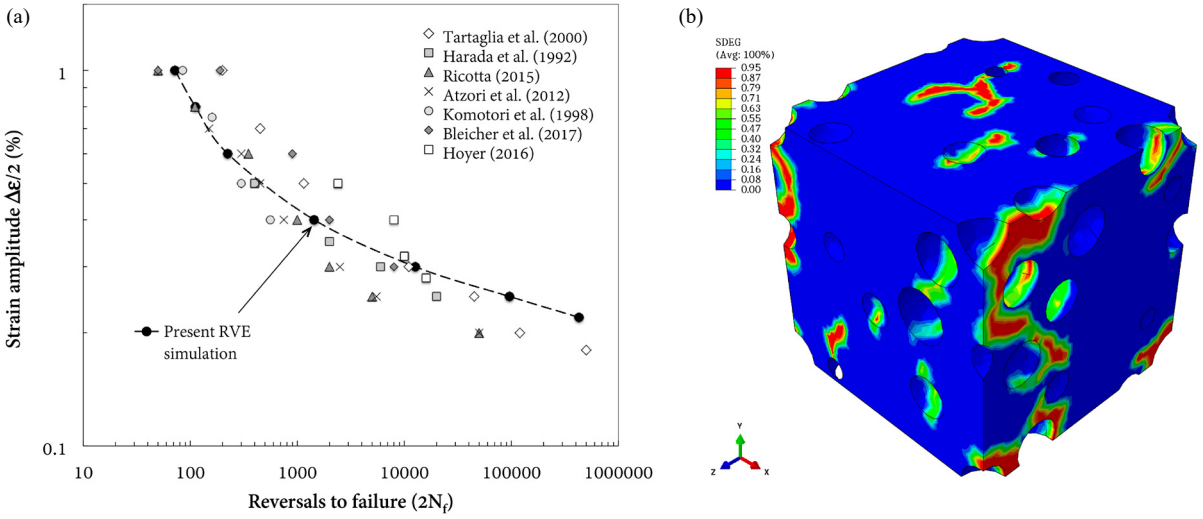

Fig. 10. (a) Low-cycle fatigue data within the RVE simulation; (b) contour of damage in a LCF analysis.

5. Conclusions

The ductile failure mechanism in ferritic DCI is here studied by a Reference Volume Element numerical modeling. The peculiar material microstructure is faithfully reproduced by a random periodic distribution of voids, and periodic boundary conditions are applied to the so-built cell.

Mechanical damage models are applied at the microscale, in which the ferrite is considered homogeneous and not defected, whilst the RVE response is being evaluated at the mesoscale by homogenization. Two distinct mechanical behaviors of the RVE are analyzed: the tensile failure, in which the stress triaxiality ratio over the cell is also being varied, and the strain-controlled, low-cycle fatigue.

Some relevant results are obtained, that can be summarized in the followings points:

- this RVE approach is an extremely powerful tool to predict the behavior at the mesoscale starting from the constitutive laws for the matrix, and at the same time to analyze specific phenomena going back to the microscale;

- the ductile cast iron is a material seriously affected by the nodule population: strain concentration and, above all, local triaxiality, are determined by dimension and spacing of nodules;
- imposed triaxiality value strongly affects the material ductility, demonstrating that, in specific circumstances (as notches), the failure strain is considerably diminished;
- the simulation of the low-cycle fatigue behavior correctly reproduces the test data, and gives any opportunity to optimize the microstructure to optimize the performances.

References

Atzori B., Meneghetti G., Ricotta M., Masaggia S., 2012. A compatible method to summarise the Low- and High-Cycle fatigue test results of ductile irons and structural steels. Workshop IGF, Forni di Sopra (UD), Italy, pp. 153–166.

Bao Y., Wierzbicki T., 2004. On fracture locus in the equivalent strain and stress triaxiality space. International Journal of Mechanical Sciences 46, 81–98.

Berdin C., Dong M.J., Prioul C., 2001. Local approach of damage and fracture toughness for nodular cast iron. Engineering Fracture Mechanics 68, 1107–1117.

Bidhar S., Kuwazuru O., Hangai Y. , Yano T., Utsunomiya T., Yoshikawa N., 2011. Empirical prediction of stress concentration factor for a pair of spherical cavities. Fourth International Conference on Modeling, Simulation and Applied Optimization – Kuala Lumpur (Malaysia).

Bleicher C., Wagener R., Kaufmann H., Melz T., 2017. Influence of different load histories on the cyclic material behavior of nodular cast iron for thick-walled application. In: The 27th Int Ocean and Polar Eng Conf. International Society of Offshore and Polar Engineers, pp. 175–83.

Bonora N., Ruggiero A., 2005. Micromechanical modeling of ductile cast iron incorporating damage. Part I: Ferritic ductile cast iron. International Journal of Solids and Structures 42, 1401–1424.

Bradley W.L., Srinivasan M.N., 1990. Fracture and fracture toughness of cast irons. International materials review 35(3).

Canzar P., Tonkovic Z., Kodvanj J., 2012. Microstructure influence on fatigue behaviour of nodular cast iron. Materials Science and Engineering A556, 88–99.

Collini L., 2010. La modellazione microstrutturale di materiali a struttura eterogenea: princìpi ed applicazioni. Frattura e Integrità Strutturale 12, 21–36.

Collini L., Nicoletto G., 2005. Determination of the relationship between microstructure and constitutive behavior of nodular cast iron with a unit cell model. Journal of Strain Analysis for Engineering Design 40(2), 107–116.

Dahlberg C.F., Öberg M., Faleskog J., 2014. Continuum modeling of nodular cast iron using a porous plastic model with pressure-sensitive matrix – experiments, model calibration & verification. Tech rep KTH Royal Institute of Technology, School of Engineering Science – Stockholm (Sweden).

Di Cocco V., Iacoviello F., Rossi A., D., Cavallini M., Natali S., 2013. Analysis of stress triaxiality influence: ferritic DCI damaging micromechanisms Acta Fracturae – Rome (Italy).

Di Cocco V., Iacoviello F., Rossi A., Iacoviello D., 2014. Macro and microscopical approach to the damaging micromechanisms analysis in a ferritic ductile cast iron. Theoretical and Applied Fracture Mechanics 69, 26–33.

Dong M.J., Prioul C., François D., 1997. Damage effect on the fracture toughness of nodular cast iron: Part I. Damage characterization and plastic flow stress modeling. Metall. Mater. Trans. A 28A, 2245–2254.

Ghahremaninezhad A., Ravi-Chandar K., 2012. Deformation and failure in nodular cast iron. Acta Materialia 60, 2359–2368.

Guillemer-Neel C., Bobet V., M. Clavel M., 1999. Cyclic deformation behaviour and Bauschinger effect in ductile cast iron. Materials Science and Engineering A272, 431–442.

Guillermer-Neel C., Feaugas X., Clavel M., 2000. Mechanical behavior and damage kinetics in nodular cast iron: Part I. Damage mechanisms. Metall. Mater. Trans. A 31A, 3063–3074.

Hafiz M., 2001. Mechanical properties of SG-iron with different matrix structure. Journal of Materials Science 36, 1293–1300.

Hamberg K., Johannesson B., Robertson A., 1997. Defect Sensitivity In Nodular Cast Iron For Safety Critical Components. European Structural Integrity Society 22, 37–47.

Harada S., Akiniwa Y., Ueda T., 1992. The effect of microstructure on the low-cycle fatigue behavior of ductile cast iron. In K.-T. Rie et al. (eds.), Low Cycle Fatigue and Elasto-Plastic Behaviour of Materials–3.

Hopperstad O.S., Børvik T., Langseth M., Labibes K., Albertini C., 2003. On the influence of stress triaxiality and strain rate on the behaviour of a structural steel. Part I. Experiments. European Journal of Mechanics A/Solids 22, 1–13.

Hoyer P., 2016. Untersuchung der Stützwirkung in Bauteilen aus Sphäroguss und Grauguss. Technische Universität Dresden.

Hradil P., Talja A., 2017. Ductility limits of high strength steels. Research report VTT-R-04741-16.

Hütter G., Zybell L., Kuna M., 2015. Micromechanisms of fracture in nodular cast iron: From experimental findings towards modeling strategies – A review. Engineering Fracture Mechanics 144, 118–141.

Johnson G.R., Cook W.H., 1985. Fracture characteristics of three metals subjected to various strains, strain rates, temperatures and pressures. Engineering Fracture Mechanics 21(1), 31–48.

Kanita T., Foresta S., Gallieta I., Mounourya V., Jeulin D, 2003. Determination of the size of the representative volume element for random composites: statistical and numerical approach. International Journal of Solids and Structures 40(13-14), 3647–3679.

Kobayashi T., 2004. Ductile cast iron. In: Strength and toughness of materials. Springer, pp. 89–110.

Komotori J., Shimizu M., 1998. Fracture mechanism of ferritic ductile cast iron in extremely low cycle fatigue. In: Rie K-T, Portella PD, editors. Low cycle fatigue and elastoplastic behaviour of materials. Netherlands: Springer, pp. 39–44.

Lacaze J., Sertucha, J., Åberg L.M., 2006. Microstructure of as-cast ferritic-pearlitic nodular cast irons. ISIJ International, 2016;56(9):1606–1615.

Lin R.C., Steglich D., W. Brocks W., Betten J., 2006. Performing RVE calculations under constant stress triaxiality for monotonous and cyclic loading. Int. J. Numer. Meth. Engng 66, 1331–1360.

Lin Y.F., Lui T.S., L. H. Chen, 1994. The effect of triaxial stress on ductility and fracture morphology of ferritic spheroidal graphite cast iron. Metallurgical and Materials Transactions A 25(4), 821–825.

Lukhi M., Kuna M., Hütter G., 2018. Numerical investigation of low cycle fatigue mechanism in nodular cast iron. International Journal of Fatigue 113, 290–298.

Manjoine M.J., 1982. Creep-rupture behavior of weldments. Welding Research Supplement, pp. 50s–57s.

Maresca G., Milella P.P., Pino G., 1997. A critical review of triaxiality based failure criteria. Procs. of IGF 13 – Cassino (Italy).

Meneghetti G., Ricotta M., Atzori B., 2014. A synthesis of the low- and medium-cycle fatigue behaviour of as cast and austempered ductile irons based on the plastic strain energy. Procedia Materials Science 3, 1173–1178.

Mirza M.S., Barton D.C., Church, P., 1996. The effect of stress triaxiality and strain-rate on the fracture characteristics of ductile materials. J. Materials Sci. 31, 453–461.

Needleman A., 1987. Continuum model for void nucleation by inclusion debonding. Journal of Applied Mechanics 54, 525–531.

Needleman A., Tvergaard, V., 1991. An analysis of dynamic, ductile crack growth in a double edge cracked specimen. International Journal of Fracture 49, 41–67.

Nicoletto G., Collini L., Konecna R., Bujnova P., 2004. Damage mechanism in ferritic-pearlitic nodular cast iron. Transactions of Famena 28(2), 19–26.

Nicoletto G., Collini L., Konecna R., Riva E., 2006. Analysis of nodular cast iron microstructures for micromechanical model development. Strain 42(2), 89–96.

Nicoletto G., Konecna R., Hadzimova B., L. Collini L., 2002. Microstructure and mechanical strength of nodular cast irons. Procs. of AIAS Conference – Parma (Italy).

Omairey S.L., Dunning P.D., Sriramula S., 2019. Development of an ABAQUS plugin tool for periodic RVE homogenisation. Engineering with Computers 35(2), 567–577.

Petrenec M., H. Tesarová H., Beran P., Šmíd M., Roupcová P., 2010. Comparison of low cycle fatigue of ductile cast irons with different matrix alloyed with nickel. Procedia Engineering 2, 2307–2316.

Rabold F., Kuna M., 2005. Cell model simulation of void growth in nodular cast iron under cyclic loading. Computational Materials Science 32, 489–497.

Richter H., 2017. Mote3D: an open-source toolbox for modelling periodic random particulate microstructures. Modelling Simul. Mater. Sci. Eng. 25(3), 035011.

Ricotta M., 2015. Simple expressions to estimate the Manson–Coffin curves of ductile cast irons. International Journal of Fatigue 78, 38–45.

Springer H.K., 2012. Mechanical characterization of nodular ductile iron. Rep. LLNL-TR-522091.

Tartaglia M., Ritter P.E., Gundlach R.B., 2000. DIS Ductile Iron Society, Research project No. 30.

Zhang K.S., Bai J.B., François D., 1999. Ductile fracture of materials with high void volume fraction. Int J Solids Struct 36(23), 3407–25.